Article

Molecular Sensing and Manipulation of Protein Oligomerization in Membrane Nanotubes with Bolaamphiphilic Foldamers

Kathrin Aftahy,○ Pedro Arrasate,○ Pavel V. Bashkirov,○ Petr I. Kuzmin, Victor Maurizot, Ivan Huc,* and Vadim A. Frolov*
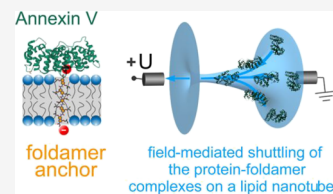
Read Online

ACCESS | 📊 Metrics & More | 📰 Article Recommendations | 🆁 Supporting Information

ABSTRACT: Adaptive and reversible self-assembly of supramolecular protein structures is a fundamental characteristic of dynamic living matter. However, the quantitative detection and assessment of the emergence of mesoscale protein complexes from small and dynamic oligomeric precursors remains highly challenging. Here, we present a novel approach utilizing a short membrane nanotube (sNT) pulled from a planar membrane reservoir as nanotemplates for molecular reconstruction, manipulation, and sensing of protein oligomerization and self-assembly at the mesoscale. The sNT reports changes in membrane shape and rigidity caused by membrane-bound proteins as variations of the ionic conductivity of the sNT lumen. To confine oligomerization to the sNT, we have designed and synthesized rigid oligoamide foldamer tapes (ROFTs). Charged ROFTs incorporate into the planar and sNT membranes, mediate protein binding to the membranes, and, driven by the luminal electric field, shuttle the bound proteins between the sNT and planar membranes. Using Annexin-V (AnV) as a prototype, we show that the sNT detects AnV oligomers shuttled into the nanotube by ROFTs. Accumulation of AnV on the sNT induces its self-assembly into a curved lattice, restricting the sNT geometry and inhibiting the material uptake from the reservoir during the sNT extension, leading to the sNT fission. By comparing the spontaneous and ROFT-mediated entry of AnV into the sNT, we reveal how intricate membrane curvature sensing by small AnV oligomers controls the lattice self-assembly. These results establish sNT-ROFT as a powerful tool for molecular reconstruction and functional analyses of protein oligomerization and self-assembly, with broad application to various membrane processes.

Annexin V / foldamer anchor / +U / field-mediated shuttling of the protein-foldamer complexes on a lipid nanotube

■ INTRODUCTION

The formation of supramolecular protein complexes with a programmable architecture through noncovalent reversible self-assembly is crucial for the spatial and functional organization of intracellular space.[1−4] This process, based on weak interactions and adaptive self-assembly, enables the dynamic tuning of the shape and material properties in protein complexes and nanostructures. The phenomenon has recently been replicated in synthetic biomaterials.[4−6] Typically, the initiation and outcomes of the self-assembly are kinetically regulated by small and dynamic oligomeric precursors.[7,8] Although our understanding of the mesoscale protein complexes and of the final products of the self-assembly has been advanced,[9,10] tracing their material properties and polymorphism back to the precursors remain experimentally challenging, hindering a comprehensive mechanistic analysis of the self-assembly process.

In the crowded intracellular environment, protein oligomerization often occurs with the involvement of membrane templates that provide various means to facilitate and regulate protein interactions.[11] Membranes can mediate protein oligomerization both in the cytosol and on their own surface.[11−13] The membrane shape is an established regulator of protein self-assembly.[11,14] Importantly, soft membrane templates are typically reshaped by emerging protein complexes. This reciprocal effect of proteins on the membrane template is implicated in cellular membrane morphogenesis.[15] Recent experiments demonstrated that membrane shape changes could reflect dynamic rearrangements of small protein subunits of a larger protein structure.[16,17] As even a single protein molecule can induce local membrane deformations, changes in the membrane shape can serve as a reporter of the self-assembly progress, spanning from the molecular scale to the mesoscale.

One technique that focuses on real-time tracking molecular-scale deformations is conductance measurements in short membrane nanotubes (sNTs) pulled from a planar membrane reservoir.[18] Through sNTs, it is possible to resolve individual and multiple binding events, as well as accompanying changes of membrane elasticity.[18,19] However, the high curvature of the sNT membrane restricts protein partitioning,[19,20] making it challenging for a random protein to accumulate and self-assemble on the sNT. Furthermore, even if protein crowding

on the sNT membrane, a step generally required to trigger self-assembly, could be achieved, it would remain difficult to discriminate the actions of individual protein oligomers as the protein ensemble would dominate the measurements. To exert control over protein partitioning and interactions on the sNT membrane and thus enable the discrimination and quantification of individual molecular complexes, we employed newly synthesized rodlike bolaamphiphile (BA) molecules. Charged BAs could be operated as primitive protein receptors mediating the membrane binding of peripheral proteins, such as annexin V (AnV), that specifically recognize charged lipid species.[21,22] Designed to traverse the sNT membrane, the BAs functioned as molecular shuttles propelled by an electric field applied to the lumen of the sNT, thereby controlling protein transfer between the sNT and the connected planar reservoir membrane. Using BA-mediated electrophoresis, we were able to detect the entry and exit of individual AnV oligomers and assess their stoichiometry and shape. Furthermore, field-driven accumulation of AnV on the sNT triggered the polymerization of a curved protein lattice encaging the sNT.[23] This protein scaffold not only stabilized the membrane within it but also mediated the sNT fission upon extension.[24,25] Comparison of the spontaneous and voltage-driven entry of AnV in sNT revealed a novel mechanism of membrane curvature sensing that AnV uses to control its membrane partitioning and polymorphic self-assembly. Altogether, our results establish BA-containing sNTs as new tools to produce, manipulate, and investigate membrane-mediated protein assemblies.

RESULTS

Design of the Shuttle BAs. Different classes of rigid synthetic BAs have been demonstrated to incorporate into a lipid bilayer and span both of its leaflets.[26] To minimally interfere with protein detection by sNTs, small lipid-sized BAs of predictable and stable shape were needed. To obtain such rigid bolalipid mimetics, we opted for oligoamide foldamers (OFs).[27−29] OFs are synthetically accessible via simple iterative amide couplings and are easy to modulate through main chain and side chain modifications. OF amphiphiles capable of incorporation into lipid membranes have been described, but applications have until now been focused on ion and water transport mediated by transmembrane helices.[30−35] Apart from relatively large helices, OF may be designed to form thinner tapelike structures of the defined length that may be converted into protein-interacting bolaamphiphiles via appropriate modification of the ends. We designed and synthesized minimal such compounds, symmetric charged rigid OF tapes (ROFTs). Compound **1** (Figure 1A) was the parent compound of a series of OF ribbons (see the Supporting Information) designed according to well-established principles validated across a vast number of OF families.[36] In this design, amide protons are engaged in intramolecular hydrogen bonds and thus unavailable for intermolecular interactions (Figure 1B). Aryl and amide units are kept coplanar, generating a linear tape with a sizable surface area for aromatic stacking. Such linear tapes have been shown to have stable conformations in a wide range of polar and nonpolar media.[36] The branched alkyl side chains appended on the edges of the tape provide a lipophilic character. However, they may not completely prevent aggregation through stacking as shown by crystal packing (Figure 1C,D). The ability of the tapes to aggregate was expected to be reduced in **4** which possesses two central decyl chains and enhanced in **2** and **3**
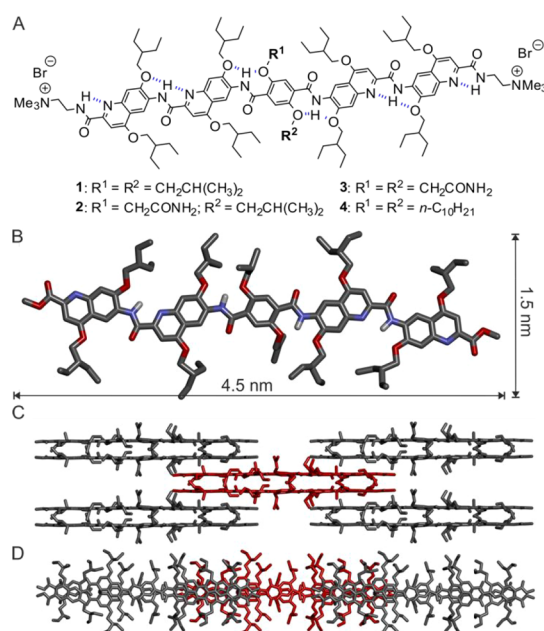
Figure 1. (A) Formula of amphipathic ROFTs **1**−**4**. Dashed lines indicate hydrogen bonds responsible for the flat shape. (B) Crystal structure of **5**, the bis-methyl-ester precursor of **1**. (C, D) Views of molecular packing in the crystal down the *c* axis (C) and down the *a* axis (D).

which instead have one or two polar primary amide appendages, respectively. The primary amides side chains are isosteric to the iBu groups of **1** but, in contrast with the iBu groups, they may engage in intermolecular hydrogen bonds within a membrane, as do asparagine residues in trans-membrane peptides.[37] All molecules are terminated with quaternary ammonium functions that give them a bolaamphiphilic nature[26] and thus potentially control their orientation within lipid bilayer membranes. While the 4.5 nm length of the ROFT molecule matches the lipid bilayer thickness, its 1.5 nm width is only slightly bigger than that of a lipid (Figure 1B). The small width in principle ensures that individual ROFTs perturb the sNTs much less than protein molecules. Compounds **1**−**4** are not soluble in water but met our expectations with respect to their insertion in membranes.

ROFTs Incorporate into Low-Curved Membrane Reservoirs and Mediate Protein Binding to the Membranes. We began testing how ROFTs incorporate and interact with the lipid bilayer using low-curved membrane templates, Giant Unilamellar Vesicles (GUVs) and their supported analogues, Giant Supported Bilayers (GSBs) suitable for fluorescence microscopy observation, and mechanical manipulations.[38] We found that ROFTs were readily incorporated into GUVs and GSBs, seen as a linear increase of the intrinsic fluorescence signal of ROFTs normalized to that of a lipid marker (Figures 2A and S1). The incorporation efficiency was the best for **4**, while it decreased from **1** to **3**, in correlation with the expected increasing propensity of ROFTs to aggregate (Figure S2). Another factor governing ROFT membrane incorporation was the lipid composition of the GSBs (Figure 2A and Table S1). Cholesterol interfered with the GSB production in the presence of ROFTs (Table S1) as it induced the formation of crystalline-like ROFT-lipid films, possibly via cholesterol-ROFT stacking. In contrast, sphingo-myelin (SM), a biological partner of cholesterol,[39] promoted
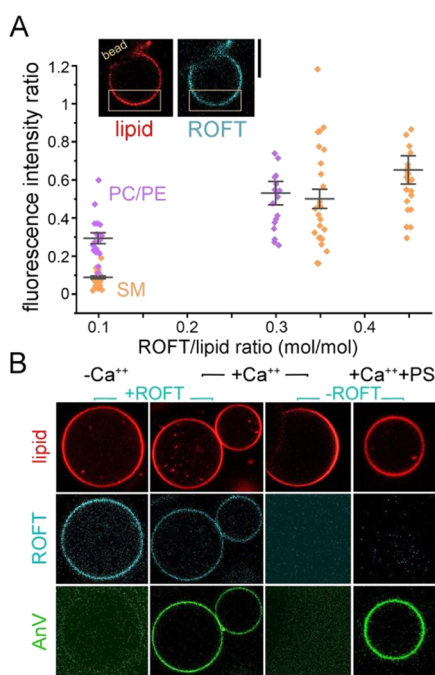
Figure 2. Membrane incorporation and AnV binding by ROFTs. (A) Incorporation of **1** into GSBs measured as the fluorescence intensity ratio F_{ROFT}/F_{lipid}, with GSBs made of SM (sphingomyelin, apricot) and PC/PE (phosphocoline/phosphoethanolamine magenta) mixtures. The inset shows a ROFT-lipid GSB attached to a silica bead; the lipid probe (Rh-DOPE, red) and the intrinsic ROFT (blue) fluorescence are seen. The rectangles delimit the region of interest (ROI) used to calculate F_{ROFT}/F_{lipid}, as the ratio of total fluorescence intensities measured upon the background subtraction. Scale bar 10 μm. (B) Ca^{2+} mediates AnV binding to GSBs containing **1** or phosphoserine (PS). The fluorescence of AnnexinV-alexa488 (green), lipid (Rhodamine-PE, red), and **1** (ROFT, blue) is seen. Scale bars 10 μm.

the incorporation of high amounts of ROFTs (Table S1 and Figure 2A). The incorporation efficiency was further improved upon the addition of cone-shaped and polyunsaturated lipids abundant in cellular membranes (Table S1). Because of these properties, we selected **1** and **4** in a simple biomimetic PC/PE lipid background for further experiments.

The sensitivity of ROFT incorporation to the composition of the hydrophobic tails of the GSB lipids suggests that the ROFTs orient along the membrane normal and span the lipid bilayer as extended bola-amphiphiles, stipulated by the highly hydrophobic aromatic core of ROFTs.[40] Accordingly, the topographic AFM scanning of supported lipid bilayers made from ROFT-containing GSBs revealed no patterns indicative of ROFTs laying parallel to the membrane interface (Figure S3). The normal orientation of ROFTs, suitable for amphiphilic self-assembly of a molecular film, was further confirmed by the formation of GSBs from detergent solutions of **4** (Figure S2C).

Upon a random testing with fluorescently labeled membrane-remodeling proteins available in house, we found that **1** and **4** (in PC/PE background) mediate membrane binding of AnV (Figure 2B), as well as other peripheral membrane proteins, namely, the epsin N-terminal homology domain and Dynamin1 (Figure S4), all known to depend upon negative membrane charge for membrane binding.[19,41] Thus, protein binding was evidenced with the first generation of ROFTs

without requiring further functionalization of their solvent exposed polar groups. The binding indicates that ROFTs create negative surface potential, in agreement with the efficient incorporation of ROFTs into purely cationic membranes and also confirmed by measurements of the membrane boundary potential changes (Table S1 and Figure S5). While both Dyn1 and AnV can self-assemble into large cylindrical structures on the sNT membrane,[23,41] the low oligomeric precursors of AnV self-assembly on a planar membrane are well characterized.[42,43] We chose AnV for further testing.

ROFTs Emulate Ca^{2+} and Curvature Dependence of AnV Membrane Binding. AnV (2 μM in the bulk) binding to GSBs containing **1** or **4** showed Ca^{2+} dependence characteristic of AnV interaction with its physiological target, PS (Figures 2B and S4).[22,43] Chelating free Ca^{2+} by EDTA caused AnV detachment from both ROFT- and PS containing GSBs (Figure S4).[44] However, in both cases, residual binding was detected (Figures 2B and S4), indicating a weak Ca^{2+}-independent binding mode. This is consistent with the overall complexity of membrane binding of annexins controlled by electrostatic and hydrophobic interactions.[21,44] We next checked how the AnV binding changes with the membrane curvature.

Micron-long NTs could be readily produced from both ROFT- and PS-containing GSBs (Figure 3A). ROFTs were visibly expelled from the NTs (Figure 3A). The ratio between
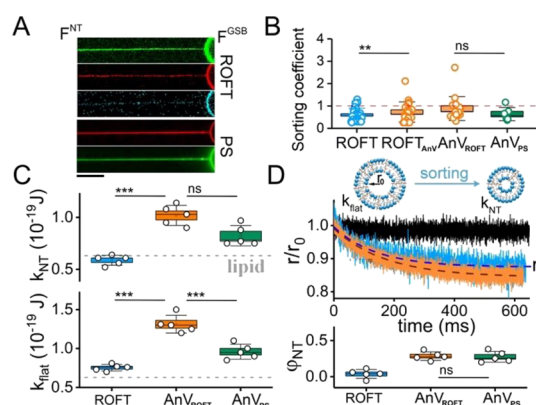
Figure 3. ROFT and AnV sorting detected by fluorescence microscopy and conductance measurements. (A) Fluorescence micrographs show AnV binding to the outer leaflet of NT containing **4** (30 mol %) or PS (30 mol %). Scale bar 10 μm. (B) Boxplot shows sorting coefficients $q = \dfrac{F_{ROFT\ or\ AnV}^{NT} F_{lipid}^{GSB}}{F_{ROFT\ or\ AnV}^{GSB} F_{lipid}^{NT}}$;[25,45] the fluorescence of ROFTs (F_{ROFT}) was used to calculate the sorting coefficient of **4** (1st and 2nd boxes) in the absence (ROFT, blue) and presence ($ROFT_{AnV}$, orange) of AnV, the fluorescence of AnV-Alexa488 was used to calculate the sorting coefficient of AnV (3rd and 4th boxes) in sNTs containing **4** (AnV_{ROFT}) or PS (AnV_{PS}). All means are significantly smaller than 1 (at $p = 0.05$). (C) Boxplots show the effective bending rigidity of sNT (upper panel) and reservoir (lower panel) membranes (see Figure S7 for details). The gray dash line shows the bending rigidity of the reference lipid membrane k_l (Figure S7).[18,19] (D) Upper panel shows kinetics of the sNT radius decrease caused by the curvature-stress-driven expulsion of **4** (blue) and AnV and **4** (apricot) from sNTs at low $U = +50$ mV. The changes are normalized to the initial sNT radius, and the control is pure lipid sNT (black). The lower panel shows φ_{NT} calculated from the rigidity changes (see the Supporting Information, Model 3.3. for details).

the ROFT concentrations (area fraction) in the GSB (φ_0) and NT (φ_{NT}), the sorting coefficient $q = \varphi_{NT}/\varphi_0$, was measured as the ratio of the fluorescence intensities (F) coming from the lipid probe (Rhodamine-PE) and the ROFTs in the NT membrane normalized to that measured in the GSB (Figures 3A and S6).[25] For both **1** and **4,** preferential partitioning into low-curved GSB, equivalent to $q < 1$, was detected (Figures 3B and S6). The ROFTs sorting away from NTs were associated with the ROFT rigidity. The sorting of a rigid membrane inclusion can be estimated as (see Supplementary Model 3.1):

$$q \approx 1 - \frac{ak_{flat}}{2k_B Tr}\left(\frac{1}{r} - 2J_s\right) \qquad (1)$$

where a is the inclusion area on the membrane surface, k_{flat} is the bending rigidity of the reservoir membrane, r is the NT radius, and J_s is the intrinsic curvature of a membrane fully covered by inclusions. Symmetric ROFT molecules oriented along the membrane normal and spanning both lipid monolayers are expected to create planar geometry with $J_s = 0$. Eq 1 then predicts a nonlinear $(\sim r^{-2})$ dependence of the ROFT partitioning into the NT on the membrane curvature, in agreement with experimental observations (Figure S6).

We next quantified q for the fluorescently labeled AnV. Following eq 1, the expulsion of the rigid inclusions from the NT shall increase with a. Surprisingly, despite the large difference in a (~30 nm^2 for AnV,[44] and 2−3 nm^2 for ROFTs, see Figure 1B) the AnV sorting was comparable with that of ROFTs on PS-containing membranes (Figure 3B, green and blue, no significant difference at $P = 0.05$). Similar weak expulsion of AnV from NT was observed on ROFT-containing membranes (Figure 3B apricot and green). Following eq 1, the diminished expulsion of AnV might be associated with a much-reduced k_{flat} or, likelier, a greater preference for the NT curvature parametrized by positive J_s. Such a preference would be consistent with membrane insertion of AnV into the hydrophobic core of the lipid bilayer,[21] seen here as the weak Ca^{2+}-independent AnV binding to both PS- and ROFT-containing membranes (Figures 2B and S4). Furthermore, a strong interaction between ROFTs and AnV, seen in significant suppression of the ROFT exit from the NTs by AnV (Figure 3B apricot and blue), implies that ROFTs might be directly engaged in the formation of the hydrophobic contacts between AnV and the membrane. We next tested whether this complex set of interactions can be unraveled by sNT conductance measurements.

Detection of the Bulk Partitioning of ROFTs and AnV into sNTs. The sNTs are shorter and thinner than the NTs pulled from GSB: the sNT length ranges from 80 nm to a few microns and the luminal radius ranges from 2 to 10 nm (Figure S7).[18] The ionic conductance through the sNT lumen measured in voltage-clamp mode is the major experimental readout. The smallest sNTs resolve the conductance changes due to molecular-scale membrane deformations. The longer micron-length tubes report the real-time changes of the average sNT radius (r) and the bending rigidity of the sNT membrane (k_{NT}) upon protein entry into or exit from the tube.[18] We note that k_{NT} here is not a material parameter but an effective rigidity modulus dependent on the molecular exchange between the reservoir and sNT membranes.[19,46] As such, it defines the sNT curvature:

$$r_s = \sqrt{\frac{k_{NT}}{2\sigma}} \qquad (2)$$

where σ is the reservoir membrane tension.[47] In the stationary state, k_{NT} can be directly measured (Figure S7).[18] We first utilized this bulk "elastic" detection mode to characterize the effect of AnV on k_{NT}.

For rigid molecules such as ROFTs or AnV, that preserve their shape during membrane deformations, k_{NT} can be related to the bending rigidity of the planar reservoir k_{flat} as

$$k_{NT} \approx k_{flat}\left(1 + \frac{3(q-1)\varphi_0}{2}\left(1 - \frac{2}{3}r_s J_s\right)\right) \qquad (3)$$

where r_s is the stationary sNT radius. The k_{NT} values approached that of the pure lipid sNT, indicating strong expulsion of **4** from sNT due to its high membrane curvature (Figure 3C, upper graph and Figure S7). To reveal the curvature dependence of k_{NT}, we substituted eq 1 into eq 2 and, assuming $J_s = 0$, we obtained $k_{NT} \approx k_{flat}\left(1 - \frac{\varepsilon}{r_s^2}\right)$. The quadratic dependence of k_{NT} on the curvature of sNT obtained experimentally with sNTs containing **4** confirmed the rigidity-driven mechanism of ROFT expulsion from sNT (Figure S7).

Eq 2 shows that the softening of the sNT membrane due to egression of **4** from the sNT is coupled to the reduction of r as

$$\frac{\Delta k}{k_{NT}} \approx 2\frac{\Delta r}{r_s} \qquad (4)$$

A gradual decrease of r indeed followed sNT formation (Figure 3D upper panel, blue, Figure S8),[19] with the amplitude $\Delta r = r_s - r_0$ estimating that of the bending rigidity $\Delta k = k_{flat} - k_{NT}$. The decrease was detected in the presence of **4** but not in the control single-lipid component tubes (Figure 3D, upper panel, black and Figure S7).[19] Using eq 4, we calculated k_{flat} from the measured k_{NT}, Δr, and r_s (Figures S7 and S8). As expected, the addition of **4** drove k_{flat} significantly above ($P < 0.01$) the bending rigidity of the reference lipid reservoir k_l (Figure 3C, lower panel,). Importantly, the k_{flat} values were similar to those obtained from the k_{NT} dependence on the sNT curvature ($0.75 \pm 0.04 \times 10^{-19}$ J, Figure 3C, analogous to $0.72 \pm 0.02 \times 10^{-19}$ J, Figure S7, at $p = 0.05$) but significantly larger than k_{NT} (at $p = 0.01$).

The rigidity increase allowed estimating the efficiency of the incorporation of **4** into the reservoir membrane: using $\varphi_0 = \frac{k_{flat} - k_l}{k_{flat}}$ (Supplementary Model 3.1),[19] we found $\varphi_0 = 0.16 \pm 0.05$. Crucially, this value closely matched the mole fraction of **4** in the membrane-forming mixture, thus further confirming the seamless incorporation of **4** into the reservoir membranes (Figure 1A). We finally used eq 3 to obtain q and φ_{NT} from the difference between k_{flat} and k_{NT} (Supplementary Models 3.1, 3.3, and eq S5). Again, in agreement with the strong expulsion of **4** from highly curved sNT, we found $\varphi_{NT} \approx 0$ (not significantly different from 0 at $p = 0.1$, Figure 3D, lower panel).

With AnV (2 μM in the bulk) bound to either **4** (20 mol %) or PS (20 mol %), the sNT bending rigidity remained much higher than that of the lipid-only sNT (Figure 3C, upper graph), in agreement with the efficient partitioning of AnV into NT reported by fluorescence microscopy (Figure 3A). AnV also augmented the amplitude of the decrease of r measured after the sNT formation (Figure 3D, upper panel, orange and

Figure S8) and, consequently, the increase of k_{flat} (Figure 3C, lower panel), thus ruling out the AnV softness as the cause of its weak expulsion from the sNT. The dependence of k_{NT} on the sNT curvature measured with AnV was more complex than with 4, with the fitting relying upon a moderately positive J_s (Figure S7).

The k_{flat} increase was similar on the 4- and PS-containing membranes ($\Delta k_{flat} \sim 4 \times 10^{-20}$ J). The φ_0 estimation yielded similar AnV coverage of the reservoir membrane for PS-containing ($\varphi_0 = 0.38 \pm 0.05$, SD $n = 5$) and 4-containing $\varphi_0 = 0.34 \pm 0.05$ (SD $n = 6$) reservoirs (Supplementary Model 3.3). In turn, the sNT coverage was found similarly lower ($\varphi_{NT} \sim 0.27$, Figure 3D, lower panel).

The weak expulsion of 4- and PS-bound AnV qualitatively agrees with the fluorescence microscopy observations (Figure 3C). Both data sets indicated that AnV could spontaneously partition into the curved membranes of the nanotubes due to a finite positive J_s. We next asked whether AnV oligomers could be moved from the planar reservoir to the sNT by ROFT-mediated electrophoresis to assess the full spectrum of their sizes and interactions.

ROFTs Enable Field-Controlled Partitioning of AnV into sNT. An electric field driving the ionic current through the sNT lumen also acts on charged molecular species in the inner leaflet of the sNT membrane (Figure 4A).[48] In the presence of 4, the increase of the voltage bias U in the lumen to +150 mV triggered a gradual growth of the sNT conductance, reversible upon the voltage decrease (Figure 4B, blue). The k_{NT} measurements at the plateau revealed that
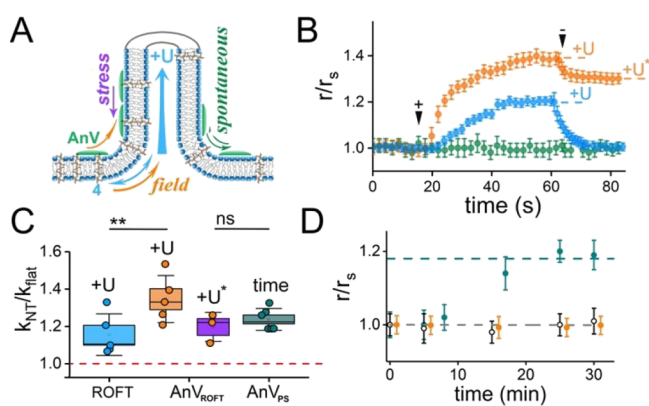
Figure 4. Field-driven partition of AnV into PS- and 4-containing sNTs. (A) Cartoon shows different pathways of molecular exchange between the reservoir membrane and the sNT: field-driven exchange mediated by 4 (blue and apricot), spontaneous (green, relevant to PS-containing membranes), and stress-driven expulsion upon switching off the voltage bias (purple). (B) Changes of r caused by the U increase to +150 mV (+arrow) followed by the decrease to +50 mV (−arrow). The sNT contains 4 (blue), 4 and AnV (apricot), and PS and AnV (green). The time points are average values obtained from 3 to 5 independent experiments. (C) Boxplot shows the k_{NT} (normalized to k_{flat}) measured upon voltage-driven expansion of ROFT-sNTs (at the +U level seen in panel B, blue), upon the expansion of ROFT-sNT with bound AnV (at the +U level seen in panel B, orange), upon the constriction of ROFT-sNT with bound AnV caused by the U decrease (at the +U* level seen in panel B, purple), and upon spontaneous expansion of the PS-NTs with bound AnV (see panel D, green). (D) Changes of r measured with PS-sNT (black, control), PS-sNTs with bound AnV (green), and ROFT-sNT with bound AnV held at $U = -50$ mV (apricot). The time points are average values obtained from 3 to 5 independent experiments.

k_{NT} increased above k_{flat} (Figure 4C, blue), in agreement with the voltage-driven accumulation of 4 in the sNT above its reservoir concentration. No sNT expansion was observed in the control experiments with sNTs containing PS and sNTs containing 4 upon the negative voltage application (Figure S9).

AnV (2 μM in the bulk) significantly enhanced the field-driven expansion of sNTs containing 4 (Figure 4B, apricot). No voltage effect was seen with AnV bound to sNTs containing PS (Figure 4B green), confirming that membrane-spanning 4 was needed to translate the electrophoretic force to the AnV bound to the outer sNT monolayer. In agreement with comigration of 4 and AnV, the kinetics of the sNT expansion in the presence of AnV ($\tau/r_{NT} = 1.4 \pm 0.3$ s/nm, Figure 4B apricot) was about twice slower than in its absence (3.5 ± 1.1 s/nm, Figure 4B, blue). Curiously, AnV could also cause spontaneous expansion of PS-containing sNT, albeit at a much slower time scale (Figure 4D, green). No slow sNT expansion was observed in the control experiments without AnV (Figure 4D, black). Similarly, no expansion of sNTs containing 4 with bound AnV was detected when a negative U (−50 mV) was applied to suppress the entry of 4-AnV complexes into the sNT (Figure 4D, orange and Figure S9). We next assessed the AnV state on the expanded sNTs.

Detection of AnV Polymerization on the sNT Membrane. Unlike with 4 alone, in the presence of AnV, the voltage-driven sNT expansion was only partially reversible (Figure 4B, +U*), implying that AnV accumulated on the sNT membrane remained there and maintained k_{NT} above k_{flat} (Figure 4C, purple). Importantly, the k_{NT} became independent of the sNT curvature indicating that the curvature-dependent exchange of AnV between the sNT and reservoir membranes was abolished (Figure S7), as AnV molecules on the sNT membrane self-assembled into an extended lattice.[23] Indeed, the sNT coverage by AnV estimated for the rigidity increase ($\varphi_{NT}^* = 0.50 \pm 0.04$, SD $n = 5$, Supplementary Model 3.3) approached that of the $p6$ lattice formed by AnV on a planar surface.[42–44]

The spontaneous expansion of PS-containing sNTs was also associated with a k_{NT} increase comparable with that observed upon the voltage reduction in sNTs (Figure 4C, purple and green). The AnV coverage increased proportionally to k_{NT} (to $\varphi_{NT}^* = 0.46 \pm 0.04$, SD $n = 6$, Supplementary Model 3.3), implying spontaneous polymerization of AnV on the PS-containing sNT. Importantly, no spontaneous sNT expansion was detected without AnV (Figure 4D, black) or when AnV bound to 4 was prevented from the sNT entry by negative U (Figure 4D, apricot).

The formation of a stable AnV lattice on the sNT membrane was further probed via variations in the sNT length. We found that the dependence of the sNT conductance (G_{NT}) on its length (L_{NT}) changed with AnV polymerization on the sNT containing 4. Prior to the polymerization (at low U), we recovered the hyperbolic $G_{NT}(L_{NT})$ characteristic for a cylinder of a constant radius r_s:[18]

$$G_{NT} \approx r_s^2/\rho_{NT}L_{NT} \tag{5}$$

This dependence shows that sNT can be freely extracted from and reinserted into the membrane reservoir (Figure 5A). Fitting $G_{NT}(L_{NT})$ obtained experimentally with eq 4 yielded the sNT radius r_s (Figure 5B, −U).[18] Upon voltage-induced formation of a stable AnV coverage on the sNT surface (Figure 4, +U*), the $G_{NT}(L_{NT})$ dependence became nonsmooth with visible jumps and inflection points, indicating a barrier for AnV
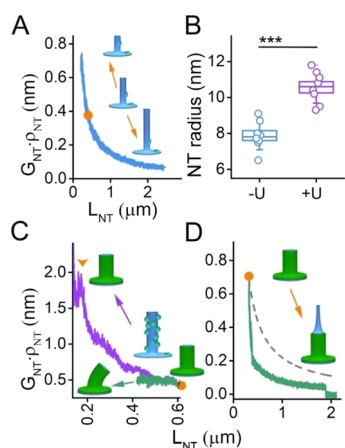
Figure 5. AnV scaffolds limit both the shortening and extension of sNT. (A) Characteristic example of $G_{NT}\rho_{NT}$ changes with the L_{NT} variations measured with sNT containing **4** and AnV prior to AnV polymerization. (B) Boxplot shows the sNT radii calculated from fitting $G_{NT}(L_{NT})$ dependences using eq 4. (C) Characteristic example of $G_{NT}\rho_{NT}$ increase with the sNT shortening measured with sNT containing **4** (purple) and PS (green) and AnV upon AnV polymerization. (D) Example of the sNT extension and fission in the presence of an AnV scaffold. The $G_{NT}(L_{NT})$ shows faster decay than that predicted by eq 4 (gray dashed line).

transfer from sNT to the reservoir (Figure 5C, purple). Fitting of the dependence yielded higher r_s (Figure 5B, +U), in agreement with the sNT expansion by AnV accumulated on the sNT membrane (Figure 4B). Furthermore, at short lengths (ranging between 90 and 220 nm), $G_{NT}(L_{NT})$ reached a plateau (Figure 5C, arrowhead), indicating the appearance of a protein scaffold encaging the sNT and preventing further decrease of the tube length (Figure 5C, purple arrow). On the PS-containing sNT, such a plateau was detected at the beginning of shortening (Figure 5C, green). In this case, the protein scaffold covering the whole sNT maintained L_{NT} and r_s, and thus G_{NT}, constant and could only bend upon the sNT shortening (Figure 5C, green path), eventually leading to tube rupture. Hence, slow spontaneous entry of AnV into sNT resulted in more complete and stable protein coverage, indicating that the formation of the AnV lattice on the sNT membrane is kinetically regulated.

Complete blockage of the sNT shortening seen on the PS-containing sNTs implied that the protein scaffold extended all the way through the transition zone between the sNT and the planar reservoir (Figure 5C, cartoon). A protein scaffold anchored to the reservoir membrane is expected to impair the lipid efflux from the reservoir during the sNT extension, with the friction between the lipids and the scaffold contributing to the constriction of the elongating sNT.[24] Indeed, we found that the extension of sNTs covered by AnV scaffolds led to fast constriction and fission (in 6 out of 6 cases, Figure 5D).

Overall, the experiments presented above demonstrated that AnV could polymerize on the highly curved membrane templates. The moderate integral rigidity of the scaffold, about 2 times bigger than that of the reference lipid bilayer (Figures 3C and 4C), enables AnV polymerization on membrane templates of different curvatures, making the scaffold a polymorphic membrane-stabilizing tool. The above results also indicate that the properties of the curved AnV lattices could be kinetically controlled via the entry of small

oligomers. We next performed single-molecule assessment of the entry process.

Detection of the Partitioning of Small AnV Oligomers into the sNT. To detect AnV entry with single-molecule resolution, we used sNTs with a length ranging from 100 to 250 nm and a radius of 6 to 8 nm.[18] Right after the increase of the voltage bias to +150 mV (see Figure 4A,B), we detected stepwise changes of the sNT conductance overlapped with an upward trend of the baseline (Figure 6A, apricot). The small
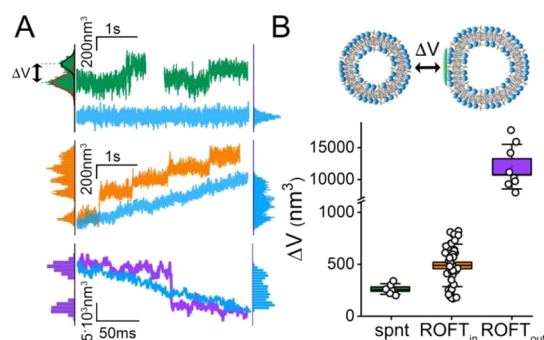
Figure 6. Detection of the entry/exit of individual AnV oligomers to/from the sNT. (A). Stepwise conductance changes were detected upon spontaneous (green) and voltage-driven (apricot) AnV entry into sNT, as well as upon AnV exit driven by the length decrease (violet). No stepwise changes were detected without AnV when sNTs contained only **4** (blue traces). (B) Boxplot shows the changes of the luminal volume of sNT corresponding to individual conductance steps seen in A; the cartoon shows how the sNT cross-section is expanded by a bound AnV monomer.

stepwise conductance increases indicated local expansion of the sNT by individual AnV monomers or oligomers entering the sNT from the planar reservoir membrane. Without AnV, the conductance of the sNTs containing **4** showed no stepwise changes upon the U increase, with the gradual growth of the conductance (Figure 6A, blue) reminiscent of that recorded with longer sNTs (Figure 4B, blue).

Similar stepwise conductance changes, albeit less frequent and reversible, were detected with PS-containing sNTs prior to AnV polymerization (Figure 6A green). As the AnV coverage of such sNTs is relatively high (Figure 3D, lower panel), the stepwise changes were interpreted as spontaneous entries and exits of AnV oligomers. The sNT conductance increase was associated with the local expansion of the sNT lumen, parametrized by the luminal volume increment (Δv, Figure 6B).[18] AnV entry produced extremely small Δv values consistent with molecular deformations (Figure 6B). Crucially, $\Delta v \varphi_U$ correctly estimated the total increase of the sNT volume upon AnV entry measured at the end of the sNT expansion (Figure 4B and Supplementary Model 3.3). Similar quantification for the steps detected during the sNT shortening (Figure 5C) yielded much bigger Δv, in agreement with the formation of small elements of the AnV lattice (Figure 6, violet)

To relate Δv to the size of AnV oligomers in the membrane plane, a simple ad hoc model for a local sNT deformation by a flat and rigid disk of area a, mimicking slightly concave AnV oligomers, was used (Supplementary Model 3.2 and Figure S10). In the linear approximation, we obtained the following equation: $a \approx \Delta v/r$. Using this approximation, we found that the Δv measured on the PS-containing sNT corresponded to

AnV monomer ($a \sim 30$ nm^2,[44]) while $\Delta\nu$ measured with **4** corresponded to a mixture of AnV monomers and trimers, known precursors of AnV polymerization of the flat surface.[42]

Comparison of spontaneous and voltage-driven entry of AnV into sNTs (Figure 6B, green and apricot) revealed that the curvature barrier between the planar reservoir membrane and the sNT is surmountable only for the smallest AnV oligomers with a comparable to the AnV monomers. The barrier is to be relatively low to account for substantial coverage of PS-containing NTs and sNTs by AnV (Figure 3B,D, lower panel). Nevertheless, using the rigid disk model, we found that, even for the smallest $\Delta\nu$ associated with AnV monomers, the barrier was around $5k_BT$, that is, prohibitively high for spontaneous crossing (Supplementary Model 3.2). As the model correctly predicted the size of AnV monomers, a correction factor not related to the molecular shape or rigidity was needed to explain the spontaneous AnV partitioning into the sNT membrane. We found that such a correction could be associated with the membrane curvature dependency of the hydrophobic interaction between AnV and lipids (Supplementary Model 3.2).[21] Interestingly, such a dependency is formally equivalent to the introduction of an effective positive J_s^* (Supplementary Model 3.2), in agreement with the experiment. We next found that with $J_s^* \sim 0.05$ nm^{-1}, the energy barrier for the AnV monomer entry to sNT reduced to the values ($\sim 2k_BT$) fully compatible with the experiment (Supplementary Model 3.2). The same J_s^* value was used to fit the dependence of k_{NT} on the sNT curvature measured on sNTs containing **4** in the presence of AnV (Figure S7). While more is to be done to unravel the complexity of AnV interactions with the lipid bilayer, these results highlight the capabilities of ROFT-sNTs in obtaining fine molecular details of the proteo-lipid interactions.

◼ DISCUSSION

The ability to create shapes through molecular self-assembly is essential in both life and technology.[5] However, few methods are available to study this process with molecular precision and establish a connection between the resulting mesoscale shapes and their elementary molecular precursors. Within cells, protein oligomerization and self-assembly can be facilitated and guided by soft membrane templates, where the shape of the membrane changes with the protein binding and self-assembly.[11,14] We showed here that the shape changes induced by AnV bound to sNTs can be used to track in real-time the oligomeric state of AnV on the sNT membrane. Both the molecular-scale deformations caused by small oligomeric precursors of AnV polymerization and the mesoscale expansion and stiffening of sNT by the AnV lattice self-assembled on the sNT surface were resolved. Simple elastic modeling indicated that the small stepwise deformations (Figure 6B) could be produced by rigid AnV oligomers, monomers, and trimers, known elementary precursors of the planar AnV lattice.[42,44] In turn, the moderate rigidity increase upon AnV accumulation on the sNT membrane indicated that these rigid oligomers self-assemble into a flexible cylindrical lattice.[23]

Spontaneous and unexpected partitioning of AnV oligomers to positively curved NTs was detected by both fluorescence microscopy and conductance measurements (Figure 3), in contrast with earlier association of their shape with negative membrane curvature.[49] Furthermore, the analysis of membrane deformations imposed by AnV oligomers confirmed their close-to-planar geometry. To explain their partitioning to NTs,

hydrophobic interaction stimulated by packing defects associated with increasing membrane curvature were invoked.[21,50] Introduction of a curvature-dependent hydrophobic interaction explained the spontaneous size-dependent entry of AnV, indicating a novel intricate mechanism of the curvature sensing by AnV relevant to the overall complexity of membrane interactions by annexins.[51] The sensing is defined by two antagonistic factors, the concave molecular shape of AnV and its interaction with the hydrophobic core of the lipid bilayer, which can be parametrized by an effective positive J_s^* (as summarized by eq 1). As a result, AnV monomers are ambivalent toward the positive mean membrane curvature: they can be both attracted to or repelled from the membrane templates of positive curvature, depending on the ratio between the membrane curvature value and J_s^*.

Spontaneous, or ROFT-assisted, partitioning of small AnV oligomers into the sNT was effective enough to enable further AnV self-assembly into a curved lattice. Importantly, the self-assembly process is kinetically controlled, with the faster ROFT-assisted assembly leading to less regular, fragmented lattices (Figures 5C and 6A, purple). The differences between the lattices forming on the sNT containing PS and **4** can be interpreted in terms of the number of nucleation events.[42,43] The slow, sigmoidal time dependence of the lattice formation on the PS-NTs (Figure 4D, green) indicates that the nucleation is a rate-limiting step, with a single nucleation event leading to the complete lattice. In turn, the AnV crowding on the sNT enforced by **4**-mediated electrophoresis triggered the formation of multiple nucleation points and, as a result, rival polymerization processes, leading to more fragmented sNT coverage.

Our major criterion for the lattice appearance was the impairment, followed by complete obstruction, of sNT retraction to the reservoir membrane (Figure 5B,C). Such obstruction, also observed by fluorescence microscopy, is characteristic for protein scaffolds encaging sNT.[17] The experiments with the sNT extension further confirmed formation of the scaffold restricting the material exchange between the reservoir membrane and the sNT. The extension caused fast constriction and fission of the sNT (Figure 5C), a behavior earlier associated with the frictional drag imposed by the protein scaffold.[24,25] The ability of AnV to form such scaffolding suggests its direct involvement in membrane fission during membrane recycling and repair.[52]

While we detected spontaneous self-assembly of AnV on the sNT membrane, synthetic ROFT BAs played a key role in the mechanistic assessment of the self-assembly process. ROFT-mediated AnV entry to sNTs from the planar membrane reservoir revealed the well-characterized small oligomeric precursors of the planar AnV lattice (Figure 6, apricot),[42,44] thus validating our detection method. In turn, the ROFT-mediated exit of AnV confirmed the oligomerization seen as the increase in the conductance signal (Figure 6, violet). Our interpretation of the conductance changes, as well as our understanding of the mechanisms of protein binding by ROFTs, are presently basic and incomplete. However, we note that the above proof-of-principle analyses were conducted using simple symmetric ROFT prototypes. Further modification of ROFTs directed toward shape/rigidity variations and chemical recognition of proteins is possible. Indeed, the control of OF shape has found extensive use in the field of molecular recognition,[53−56] and several reports describe OF self-assembly into vesicles, fibers, gels, and liquid crystals.[57−65]

Controlled alterations of the shape and molecular rigidity of ROFT could reveal how local mechanical properties of the membrane change upon protein adsorption and, in turn, affect the protein functions. The shape flexibility might further encode complex responses to membrane stresses,[66,67] with additional experimental readouts and means of regulation of the ROFT membrane partitioning enabled.

CONCLUSIONS

Label-free real-time interrogation of protein interactions is imperative for understanding their functions in the cell and unraveling complex and dynamic protein interactomes. Here, we showed that tiny lipid membrane nanotubes constricted to almost molecular dimensions and equipped with ROFTs can be operated as primitive externally controlled nanoreactors able to contain, drive, and report on protein interactions at the membrane surface. In its simplest form, the ROFT-sNT prototype demonstrated its capabilities to resolve molecular details of AnV oligomerization and membrane interactions. Advancing the ROFT chemistry, sNT design, and the means of the interpretation of the current changes detected by the ROFT-sNT shall greatly expand its detection capabilities, potentially making it a highly selective tool for affinity and size recognition of molecular species and investigation of their interactions on and with the membrane.

ASSOCIATED CONTENT

Supporting Information

The Supporting Information is available free of charge at https://pubs.acs.org/doi/10.1021/jacs.3c05753.

> Experimental procedures and characterization of new compounds, materials and methods, and additional biophysical experiments (PDF)

Accession Codes

CCDC 2080180−2080181 contain the supplementary crystallographic data for this paper. These data can be obtained free of charge via www.ccdc.cam.ac.uk/data_request/cif, or by emailing data_request@ccdc.cam.ac.uk, or by contacting The Cambridge Crystallographic Data Centre, 12 Union Road, Cambridge CB2 1EZ, UK; fax: +44 1223 336033.

AUTHOR INFORMATION

Corresponding Authors

Ivan Huc − *Department of Pharmacy, Ludwig-Maximilians-Universität München, Munich 81377, Germany;* orcid.org/0000-0001-7036-9696; Email: ivan.huc@cup.lmu.de

Vadim A. Frolov − *Ikerbasque, Basque Foundation for Science, Bilbao 48009, Spain; Department of Biochemistry and Molecular Biology and Biofisika Institute (CSIC, UPV/EHU), University of the Basque Country, Leioa 48940, Spain;* Email: vadim.frolov@ehu.eus

Authors

Kathrin Aftahy − *Department of Pharmacy, Ludwig-Maximilians-Universität München, Munich 81377, Germany*

Pedro Arrasate − *Biofisika Institute (CSIC, UPV/EHU) and Department of Biochemistry and Molecular Biology, University of the Basque Country, Leioa 48940, Spain*

Pavel V. Bashkirov − *Research Institute for Systems Biology and Medicine, Moscow 117246, Russia*

Petr I. Kuzmin − *A.N. Frumkin Institute of Physical Chemistry and Electrochemistry, Moscow 119071, Russia*

Victor Maurizot − *Univ. Bordeaux, CNRS, Bordeaux Institut National Polytechnique, CBMN (UMR 5248), Pessac 33600, France;* orcid.org/0000-0001-6104-796X

Complete contact information is available at:
https://pubs.acs.org/10.1021/jacs.3c05753

Author Contributions

○K.A., P.A., and P.V.B. contributed equally.

Notes

The authors declare no competing financial interest.

ACKNOWLEDGMENTS

REFERENCES

(1) Wang, F.; Burrage, A. M.; Postel, S.; Clark, R. E.; Orlova, A.; Sundberg, E. J.; Kearns, D. B.; Egelman, E. H. A Structural Model of Flagellar Filament Switching across Multiple Bacterial Species. *Nat. Commun.* **2017**, *8* (1), 960.

(2) Unger, E.; Böhm, K. J.; Vater, W. Structural Diversity and Dynamics of Microtubules and Polymorphic Tubulin Assemblies. *Electron Microsc. Rev.* **1990**, *3* (2), 355−395.

(3) Mesarec, L.; Drab, M.; Penič, S.; Kralj-Iglič, V.; Iglič, A. On the Role of Curved Membrane Nanodomains, and Passive and Active Skeleton Forces in the Determination of Cell Shape and Membrane Budding. *Int. J. Mol. Sci.* **2021**, *22* (5), 2348.

(4) Gao, C.; Chen, G. Exploring and Controlling the Polymorphism in Supramolecular Assemblies of Carbohydrates and Proteins. *Acc. Chem. Res.* **2020**, *53* (4), 740−751.

(5) Luo, Q.; Hou, C.; Bai, Y.; Wang, R.; Liu, J. Protein Assembly: Versatile Approaches to Construct Highly Ordered Nanostructures. *Chem. Rev.* **2016**, *116* (22), 13571−13632.

(6) McManus, J. J.; Charbonneau, P.; Zaccarelli, E.; Asherie, N. The Physics of Protein Self-Assembly. *Curr. Opin. Colloid Interface Sci.* **2016**, *22*, 73−79.

(7) Pak, A. J.; Grime, J. M. A.; Sengupta, P.; Chen, A. K.; Durumeric, A. E. P.; Srivastava, A.; Yeager, M.; Briggs, J. A. G.; Lippincott-Schwartz, J.; Voth, G. A. Immature HIV-1 Lattice Assembly Dynamics Are Regulated by Scaffolding from Nucleic Acid and the Plasma Membrane. *Proc. Natl. Acad. Sci. U. S. A.* **2017**, *114* (47), E10056−E10065.

(8) Pellarin, R.; Schuetz, P.; Guarnera, E.; Caflisch, A. Amyloid Fibril Polymorphism Is under Kinetic Control. *J. Am. Chem. Soc.* **2010**, *132* (42), 14960−14970.

(9) Kochovski, Z.; Chen, G.; Yuan, J.; Lu, Y. Cryo-Electron Microscopy for the Study of Self-Assembled Poly(Ionic Liquid) Nanoparticles and Protein Supramolecular Structures. *Colloid Polym. Sci.* **2020**, *298* (7), 707−717.

(10) Heddle, J. G.; Chakraborti, S.; Iwasaki, K. Natural and Artificial Protein Cages: Design, Structure and Therapeutic Applications. *Curr. Opin. Struct. Biol.* **2017**, *43*, 148−155.

(11) Zhu, J.; Avakyan, N.; Kakkis, A.; Hoffnagle, A. M.; Han, K.; Li, Y.; Zhang, Z.; Choi, T. S.; Na, Y.; Yu, C.-J.; Tezcan, F. A. Protein Assembly by Design. *Chem. Rev.* **2021**, *121* (22), 13701−13796.

(12) Majewski, J.; Jones, E. M.; Vander Zanden, C. M.; Biernat, J.; Mandelkow, E.; Chi, E. Y. Lipid Membrane Templated Misfolding and Self-Assembly of Intrinsically Disordered Tau Protein. *Sci. Rep.* **2020**, *10* (1), 13324.

(13) Hu, R.; Diao, J.; Li, J.; Tang, Z.; Li, X.; Leitz, J.; Long, J.; Liu, J.; Yu, D.; Zhao, Q. Intrinsic and Membrane-Facilitated α-Synuclein Oligomerization Revealed by Label-Free Detection through Solid-State Nanopores. *Sci. Rep.* **2016**, *6*, 20776.

(14) Bozelli, J. C. J.; Epand, R. M. Membrane Shape and the Regulation of Biological Processes. *J. Mol. Biol.* **2020**, *432* (18), 5124−5136.

(15) Antonny, B. Membrane Deformation by Protein Coats. *Curr. Opin. Cell Biol.* **2006**, *18* (4), 386−394.

(16) Tagiltsev, G.; Haselwandter, C. A.; Scheuring, S. Nanodissected Elastically Loaded Clathrin Lattices Relax to Increased Curvature. *Sci. Adv.* **2021**, *7* (33), No. eabg9934.

(17) Shnyrova, A. V.; Bashkirov, P. V.; Akimov, S. A.; Pucadyil, T. J.; Zimmerberg, J.; Schmid, S. L.; Frolov, V. A. Geometric Catalysis of Membrane Fission Driven by Flexible Dynamin Rings. *Science* **2013**, *339* (6126), 1433−1436.

(18) Bashkirov, P. V.; Kuzmin, P. I.; Chekashkina, K.; Arrasate, P.; Vera Lillo, J.; Shnyrova, A. V.; Frolov, V. A. Reconstitution and Real-Time Quantification of Membrane Remodeling by Single Proteins and Protein Complexes. *Nat. Protoc.* **2020**, *15* (8), 2443−2469.

(19) Bashkirov, P. V.; Kuzmin, P. I.; Vera Lillo, J.; Frolov, V. A. Molecular Shape Solution for Mesoscopic Remodeling of Cellular Membranes. *Annu. Rev. Biophys.* **2022**, *51*, 473−497.

(20) Antonny, B. Mechanisms of Membrane Curvature Sensing. *Annu. Rev. Biochem.* **2011**, *80*, 101−123.

(21) Jeppesen, B.; Smith, C.; Gibson, D. F.; Tait, J. F. Entropic and Enthalpic Contributions to Annexin V-Membrane Binding: A Comprehensive Quantitative Model. *J. Biol. Chem.* **2008**, *283* (10), 6126−6135.

(22) Lu, J.; Le Brun, A. P.; Chow, S. H.; Shiota, T.; Wang, B.; Lin, T.-W.; Liu, G.-S.; Shen, H.-H. Defining the Structural Characteristics of Annexin V Binding to a Mimetic Apoptotic Membrane. *Eur. Biophys. J.* **2015**, *44* (8), 697−708.

(23) Wilson-Kubalek, E. M.; Brown, R. E.; Celia, H.; Milligan, R. A. Lipid Nanotubes as Substrates for Helical Crystallization of Macromolecules. *Proc. Natl. Acad. Sci. U. S. A.* **1998**, *95* (14), 8040−8045.

(24) Simunovic, M.; Manneville, J. B.; Renard, H. F.; Evergren, E.; Raghunathan, K.; Bhatia, D.; Kenworthy, A. K.; Voth, G. A.; Prost, J.; McMahon, H. T.; Johannes, L.; Bassereau, P.; Callan-Jones, A. Friction Mediates Scission of Tubular Membranes Scaffolded by BAR Proteins. *Cell* **2017**, *170* (1), 172−184.

(25) Espadas, J.; Pendin, D.; Bocanegra, R.; Escalada, A.; Misticoni, G.; Trevisan, T.; Velasco del Olmo, A.; Montagna, A.; Bova, S.; Ibarra, B.; Kuzmin, P. I.; Bashkirov, P. V.; Shnyrova, A. V.; Frolov, V. A.; Daga, A. Dynamic Constriction and Fission of Endoplasmic Reticulum Membranes by Reticulon. *Nat. Commun.* **2019**, *10* (1), 5327.

(26) Fuhrhop, J.-H.; Wang, T. Bolaamphiphiles. *Chem. Rev.* **2004**, *104* (6), 2901−2938.

(27) Gong, B. Hollow Crescents, Helices, and Macrocycles from Enforced Folding and Folding-Assisted Macrocyclization. *Acc. Chem. Res.* **2008**, *41* (10), 1376−1386.

(28) Saraogi, I.; Hamilton, A. D. Recent Advances in the Development of Aryl-Based Foldamers. *Chem. Soc. Rev.* **2009**, *38* (6), 1726−1743.

(29) Huc, I. Aromatic Oligoamide Foldamers. *Eur. J. Org. Chem.* **2004**, *2004* (1), 17−29.

(30) Qi, S.; Zhang, C.; Yu, H.; Zhang, J.; Yan, T.; Lin, Z.; Yang, B.; Dong, Z. Foldamer-Based Potassium Channels with High Ion Selectivity and Transport Activity. *J. Am. Chem. Soc.* **2021**, *143* (9), 3284−3288.

(31) Roy, A.; Joshi, H.; Ye, R.; Shen, J.; Chen, F.; Aksimentiev, A.; Zeng, H. Polyhydrazide-Based Organic Nanotubes as Efficient and Selective Artificial Iodide Channels. *Angew. Chem., Int. Ed.* **2020**, *59* (12), 4806−4813.

(32) Shen, J.; Fan, J.; Ye, R.; Li, N.; Mu, Y.; Zeng, H. Polypyridine-Based Helical Amide Foldamer Channels: Rapid Transport of Water and Protons with High Ion Rejection. *Angew. Chem., Int. Ed. Engl.* **2020**, *59* (32), 13328−13334.

(33) Lang, C.; Deng, X.; Yang, F.; Yang, B.; Wang, W.; Qi, S.; Zhang, X.; Zhang, C.; Dong, Z.; Liu, J. Highly Selective Artificial Potassium Ion Channels Constructed from Pore-Containing Helical Oligomers. *Angew. Chem., Int. Ed. Engl.* **2017**, *56* (41), 12668−12671.

(34) Wei, X.; Zhang, G.; Shen, Y.; Zhong, Y.; Liu, R.; Yang, N.; Al-Mkhaizim, F. Y.; Kline, M. A.; He, L.; Li, M.; Lu, Z.-L.; Shao, Z.; Gong, B. Persistent Organic Nanopores Amenable to Structural and Functional Tuning. *J. Am. Chem. Soc.* **2016**, *138* (8), 2749−2754.

(35) Gong, B.; Shao, Z. Self-Assembling Organic Nanotubes with Precisely Defined, Sub-Nanometer Pores: Formation and Mass Transport Characteristics. *Acc. Chem. Res.* **2013**, *46* (12), 2856−2866.

(36) Zhang, D.-W.; Zhao, X.; Hou, J.-L.; Li, Z.-T. Aromatic Amide Foldamers: Structures, Properties, and Functions. *Chem. Rev.* **2012**, *112* (10), 5271−5316.

(37) Choma, C.; Gratkowski, H.; Lear, J. D.; DeGrado, W. F. Asparagine-Mediated Self-Association of a Model Transmembrane Helix. *Nat. Struct. Biol.* **2000**, *7* (2), 161−166.

(38) Velasco-Olmo, A.; Ormaetxea Gisasola, J.; Martinez Galvez, J. M.; Vera Lillo, J.; Shnyrova, A. V. Combining Patch-Clamping and Fluorescence Microscopy for Quantitative Reconstitution of Cellular Membrane Processes with Giant Suspended Bilayers. *Sci. Rep.* **2019**, *9* (1), 7255.

(39) García-Arribas, A. B.; Alonso, A.; Goñi, F. M. Cholesterol Interactions with Ceramide and Sphingomyelin. *Chem. Phys. Lipids* **2016**, *199*, 26−34.

(40) Werner, S.; Ebenhan, J.; Poppe, M.; Poppe, S.; Ebert, H.; Tschierske, C.; Bacia, K. Effects of Lateral and Terminal Chains of X-Shaped Bolapolyphiles with Oligo(Phenylene Ethynylene) Cores on Self-Assembly Behavior. Part 2: Domain Formation by Self-Assembly in Lipid Bilayer Membranes. *Polymers* **2017**, *9* (10), 471.

(41) Schmid, S. L.; Frolov, V. A. Dynamin: Functional Design of a Membrane Fission Catalyst. *Annu. Rev. Cell Dev. Biol.* **2011**, *27* (1), 79−105.

(42) Richter, R. P.; Him, J. L. K.; Tessier, B.; Tessier, C.; Brisson, A. R. On the Kinetics of Adsorption and Two-Dimensional Self-Assembly of Annexin A5 on Supported Lipid Bilayers. *Biophys. J.* **2005**, *89* (5), 3372−3385.

(43) Lin, Y.-C.; Chipot, C.; Scheuring, S. Annexin-V Stabilizes Membrane Defects by Inducing Lipid Phase Transition. *Nat. Commun.* **2020**, *11* (1), 230.

(44) Miyagi, A.; Chipot, C.; Rangl, M.; Scheuring, S. High-Speed Atomic Force Microscopy Shows That Annexin V Stabilizes Membranes on the Second Timescale. *Nat. Nanotechnol.* **2016**, *11* (9), 783−790.

(45) Capraro, B. R.; Yoon, Y.; Cho, W.; Baumgart, T. Curvature Sensing by the Epsin N-Terminal Homology Domain Measured on Cylindrical Lipid Membrane Tethers. *J. Am. Chem. Soc.* **2010**, *132* (4), 1200−1201.

(46) Tian, A.; Baumgart, T. Sorting of Lipids and Proteins in Membrane Curvature Gradients. *Biophys. J.* **2009**, *96* (7), 2676−2688.

(47) Frolov, V. A.; Lizunov, V. A.; Dunina-Barkovskaya, A. Y.; Samsonov, A. V.; Zimmerberg, J. Shape Bistability of a Membrane Neck: A Toggle Switch to Control Vesicle Content Release. *Proc. Natl. Acad. Sci. U. S. A.* **2003**, *100* (15), No. 2962100.

(48) Chekashkina, K. V.; Galimzyanov, T. R.; Kuzmin, P. I.; Akimov, S. A.; Romanov, S. A.; Pozmogova, G. E.; Klinov, D. V.; Bashkirov, P. V. Detection of DNA Molecules in a Lipid Nanotube Channel in the Low Ion Strength Conditions. *Biochem. (Moscow), Suppl. Ser. A: Membr. Cell Biol.* **2017**, *11* (3), 217−224.

(49) Oling, F.; Santos, J. S.; Govorukhina, N.; Mazères-Dubut, C.; Bergsma-Schutter, W.; Oostergetel, G.; Keegstra, W.; Lambert, O.;

Lewit-Bentley, A.; Brisson, A. Structure of Membrane-Bound Annexin A5 Trimers: A Hybrid Cryo-EM - X-Ray Crystallography Study. *J. Mol. Biol.* **2000**, *304* (4), 561−573.

(50) Bigay, J.; Antonny, B. Curvature, Lipid Packing, and Electrostatics of Membrane Organelles: Defining Cellular Territories in Determining Specificity. *Dev. Cell* **2012**, *23* (5), 886−895.

(51) Rescher, U.; Gerke, V. Annexins − Unique Membrane Binding Proteins with Diverse Functions. *J. Cell Sci.* **2004**, *117* (13), 2631−2639.

(52) Cooper, S. T.; McNeil, P. L. Membrane Repair: Mechanisms and Pathophysiology. *Physiol. Rev.* **2015**, *95* (4), 1205−1240.

(53) Ferrand, Y.; Huc, I. Designing Helical Molecular Capsules Based on Folded Aromatic Amide Oligomers. *Acc. Chem. Res.* **2018**, *51* (4), 970−977.

(54) Plante, J. P.; Burnley, T.; Malkova, B.; Webb, M. E.; Warriner, S. L.; Edwards, T. A.; Wilson, A. J. Oligobenzamide Proteomimetic Inhibitors of the P53-HDM2 Protein-Protein Interaction. *Chem. Commun.* **2009**, *34*, 5091−5093.

(55) Reddy, P. S.; Langlois d'Estaintot, B.; Granier, T.; Mackereth, C. D.; Fischer, L.; Huc, I. Structure Elucidation of Helical Aromatic Foldamer-Protein Complexes with Large Contact Surface Areas. *Chemistry* **2019**, *25* (47), 11042−11047.

(56) Liu, Y.; Parks, F. C.; Sheetz, E. G.; Chen, C.-H.; Flood, A. H. Polarity-Tolerant Chloride Binding in Foldamer Capsules by Programmed Solvent-Exclusion. *J. Am. Chem. Soc.* **2021**, *143* (8), 3191−3204.

(57) Cai, W.; Wang, G.-T.; Xu, Y.-X.; Jiang, X.-K.; Li, Z.-T. Vesicles and Organogels from Foldamers: A Solvent-Modulated Self-Assembling Process. *J. Am. Chem. Soc.* **2008**, *130* (22), 6936−6937.

(58) Sawato, T.; Arisawa, M.; Yamaguchi, M. Reversible Formation of Self-Assembly Gels Containing Giant Vesicles in Trifluoromethyl-benzene Using Oxymethylenehelicene Oligomers with Terminal C16 Alkyl Groups. *Bull. Chem. Soc. Jpn.* **2020**, *93* (12), 1497−1503.

(59) Yan, T.; Li, F.; Tian, J.; Wang, L.; Luo, Q.; Hou, C.; Dong, Z.; Xu, J.; Liu, J. Biomimetic Pulsating Vesicles with Both PH-Tunable Membrane Permeability and Light-Triggered Disassembly−Re-Assembly Behaviors Prepared by Supra-Amphiphilic Helices. *ACS Appl. Mater. Interfaces* **2019**, *11* (34), 30566−30574.

(60) Chen, Y.; Zhao, Z.; Bian, Z.; Jin, R.; Kang, C.; Qiu, X.; Guo, H.; Du, Z.; Gao, L. Hexagonal Lyotropic Liquid Crystal from Simple "Abiotic" Foldamers. *ChemistryOpen* **2016**, *5* (4), 386−394.

(61) He, Y.; Xu, M.; Gao, R.; Li, X.; Li, F.; Wu, X.; Xu, D.; Zeng, H.; Yuan, L. Two-Component Supramolecular Gels Derived from Amphiphilic Shape-Persistent Cyclo[6]Aramides for Specific Recognition of Native Arginine. *Angew. Chem., Int. Ed. Engl.* **2014**, *53* (44), 11834−11839.

(62) Gan, Q.; Wang, Y.; Jiang, H. Twisted Helical Microfibers by Hierarchical Self-Assembly of an Aromatic Oligoamide Foldamer. *Chin. J. Chem.* **2013**, *31* (5), 651−656.

(63) Yang, Y.; Feng, W.; Hu, J.; Zou, S.; Gao, R.; Yamato, K.; Kline, M.; Cai, Z.; Gao, Y.; Wang, Y.; Li, Y.; Yang, Y.; Yuan, L.; Zeng, X. C.; Gong, B. Strong Aggregation and Directional Assembly of Aromatic Oligoamide Macrocycles. *J. Am. Chem. Soc.* **2011**, *133* (46), 18590−18593.

(64) Cuccia, L. A.; Ruiz, E.; Lehn, J.-M.; Homo, J.-C.; Schmutz, M. Helical Self-Organization and Hierarchical Self-Assembly of an Oligoheterocyclic Pyridine−Pyridazine Strand into Extended Supramolecular Fibers. *Chem. − Eur. J.* **2002**, *8* (15), 3448−3457.

(65) Zhou, C.; Cai, W.; Wang, G.-T.; Zhao, X.; Li, Z.-T. Hydrogen-Bonded Shape-Persistent Aryl Hydrazide Polymers: Side-Chain-Tuned Formation of Vesicles and Organogels. *Macromol. Chem. Phys.* **2010**, *211* (19), 2090−2101.

(66) Piazzolla, F.; Mercier, V.; Assies, L.; Sakai, N.; Roux, A.; Matile, S. Fluorescent Membrane Tension Probes for Early Endosomes. *Angew. Chem., Int. Ed. Engl.* **2021**, *60* (22), 12258−12263.

(67) Colom, A.; Derivery, E.; Soleimanpour, S.; Tomba, C.; Molin, M. D.; Sakai, N.; González-Gaitán, M.; Matile, S.; Roux, A. A Fluorescent Membrane Tension Probe. *Nat. Chem.* **2018**, *10* (11), 1118−1125.